

Dependence Between Standard Deviation and Measurement Length for C-Band Backscattering Signatures of the Baltic Sea Ice

Marko P. Mäkynen, *Member, IEEE*, Markku H. Similä, A. Terhikki Manninen, Martti T. Hallikainen, *Fellow, IEEE*, and Juha A. Karvonen

Abstract—This paper studies whether the standard deviation (std) of the Baltic Sea ice backscattering coefficient (σ°) depends on the length of measurement (l). For many kinds of surfaces, especially for a fractal one, this is the case. The study was conducted using one-dimensional C-band helicopter-borne scatterometer data and ENVISAT synthetic aperture radar (SAR) images. The results with both data sets indicate mostly a strong linear dependence between $\ln(l)$ and $\ln(\text{std}(\sigma^\circ))$ up to a distance of at least a few kilometers. Based on the analysis of empirical and simulated data (fractal and nonfractal profiles), it seems that sea ice σ° as a function of l is not completely described either by fractional Brownian motion or by a process with a single-scale autocorrelation function. Neither can the values of σ° be regarded as samples from only one probability distribution. The regression coefficients describing the dependency of $\ln(l)$ versus $\ln(\text{std}(\sigma^\circ))$ do not discriminate various ice types better than just mean and std of σ° . However, the use of regression coefficients instead of mean and std is preferred due to their scale-invariant comparability with the results of other studies. The dependence of $\text{std}(\sigma^\circ)$ on l should also be taken generally into account in the data analysis, e.g., when constructing classifiers for sea ice SAR data.

Index Terms—Fractals, sea ice, standard deviation, synthetic aperture radar (SAR).

I. INTRODUCTION

THE BALTIC Sea is a semi-enclosed brackish sea water basin where seasonal ice cover exists from the beginning of November to the end of May. Surface roughness measurements of various Baltic Sea ice types have indicated the fractal-like nature of the ice surface [1]. In general, the fractal-like nature of the surface roughness has been observed for many natural surfaces, e.g., for cultivated soil in [2] and [3]. In this paper, we study by means of data analysis if this fractal-like nature extends from a property of surface to a property of backscattering coefficient (σ°). Empirical studies performed for several synthetic aperture radar (SAR) data sets measured over many natural targets suggest that this could be the case, e.g., [4]. Additionally, for sea surface, it has been theoretically demon-

strated that the scattered signal retains some fractal characteristic of the sea fractal surface [5]. Our aim in data analysis was to determine if the root mean square (rms) variation of the Baltic Sea ice σ° data depends on the length of measurement. For a fractal surface, this is the case. The results indicated the presence of this dependence. Hence, we assessed its usability for the classification of the ice types in the SAR images. The identification of different ice types [e.g., new ice, deformed ice (DI)] which have different surface roughness statistics is very important for winter ship navigation in the Baltic Sea. In our analysis, we used C-band data acquired with a helicopter-borne Helsinki University of Technology Scatterometer (HUTSCAT) and ENVISAT Advanced SAR (ASAR) images.

II. HUTSCAT INSTRUMENT AND DATA SETS

A. HUTSCAT Instrument

The HUTSCAT is a helicopter-borne nonimaging frequency modulated carrier wave (FM-CW) scatterometer that operates simultaneously at 5.4 and 9.8 GHz (C-band and X-band) with all four linear polarizations [6]. At each channel, 20 backscattered power spectra per second are measured. The range resolution of the spectra is 0.68 m. Simultaneous with the backscattering measurements, the target is recorded by a video camera. A typical flight altitude is 100 m, and the flight speed is 25 m/s. At 5.4 GHz, the 90% confidence interval of the absolute σ° is better than ± 0.8 dB. The noise equivalent σ° at 5.4 GHz is less than -28 dB for copolarizations and less than -44 dB for cross polarizations.

B. HUTSCAT Data Set

HUTSCAT data were acquired during seven ice research campaigns from 1992 to 2003. R/V Aranda operated by the Finnish Institute of Marine Research was the base for the HUTSCAT and ground truth measurements. HUTSCAT measurements were conducted at incidence angles of 23° and 45° along selected test lines that included various ice types. A typical length of each test line was tens of kilometers.

Seventy-seven percent of the total HUTSCAT data corresponding to a distance of around 1000 km was assigned into various ice-type classes by video imagery. The ice-type classes are based on the classification used operationally for the Finnish ice charts and also on the Baltic Sea ice code [7]. The ice-type classes are as follows: Nilas (NI) is a general term for recently formed ice that is usually less than 10 cm thick. Smooth level ice (SLI) is almost unaffected by deformation: only cracking or

Manuscript received April 22, 2005; revised March 9, 2006. This work was supported by the Finnish Funding Agency for Technology and Innovation under Project "ENVISAT and the Baltic Sea Ice Conditions."

M. P. Mäkynen and M. T. Hallikainen are with the Laboratory of Space Technology, Helsinki University of Technology, FIN-02015 TKK Espoo, Finland (e-mail: marko.makynen@tkk.fi; martti.hallikainen@tkk.fi).

M. H. Similä and J. A. Karvonen are with the Finnish Institute of Marine Research, FIN-00561 Helsinki, Finland (e-mail: markku.simila@fmr.fi; juhak@kuohu.fmr.fi).

A. T. Manninen is with the Finnish Meteorological Institute, FIN-00101 Helsinki, Finland (e-mail: terhikki.manninen@fmi.fi).

Digital Object Identifier 10.1109/TGRS.2006.875774

TABLE I
ENVISAT SAR IMAGES ACQUIRED OVER THE NORTHERN PART
OF THE BAY OF BOTHNIA IN FEBRUARY 2003

Date&Time [UTC]	Image & Swath	Polarization	Image Centre	Incidence Angle	Looks az x range	Snow Cover
14 Feb 11:01	IMP IS3	HH	N64.89 E24.99	25.8-31.2	4 x 1	Dry
15 Feb 21:59	APP IS6	HH HV	N64.70 E24.50	39.0-42.7	2 x 3	Dry
16 Feb 21:28	IMP IS1	HH	N64.82 E24.61	14.3-22.2	4 x 1	Moist
19 Feb 21:33	APP IS2	HH HV	N64.98 E24.31	18.7-26.1	2 x 1	Dry

finger rafting may occur. Rough level ice (RLI) has protruding ice blocks and floe edges and low uneven surface areas, and has typically broken and frozen several times. Slightly deformed ice (SDI) consists of ice ridges, uneven surfaces, and level ice (LI) areas, the sizes of which are usually larger than the pixel size in SAR images. The average size of LI areas in highly deformed ice (HDI) is usually smaller than the pixel size, and the proportion of LI areas is smaller than in SDI, i.e., the degree of deformation is higher. Discrimination of SDI from HDI in video imagery is often difficult and subjective. Loose and frozen brash ice (LBI and FBI) are accumulations of ice fragments not more than 2 m across. Their surface is very rough in scales below few tens of centimeters.

Ground truth data provided further classification into the following snow cover categories: 1) dry snow; 2) moist snow (volumetric wetness < 1%); and 3) wet snow (wetness > 1%). According to Hallikainen *et al.* [8], penetration depth in snow decreases rapidly as a function of snow wetness for wetness values below 1%. The decrease is much slower as the wetness is above this value. Under the wet snow condition, data exist only for SDI, HDI, and FBI. Only the dry snow condition has SLI data.

C. ENVISAT Data Set

During a sea ice field campaign in February 2003, two ENVISAT ASAR image mode precision (IMP) images at HH-polarization and two alternating polarization precision (APP) images at HH/HV-polarization were acquired over the northern part of the Bay of Bothnia (see Table I). In the delivered images, the pixel size is 12.5 m, and the geometric resolution is from 22–37 m, depending on image swath type and incidence angle [9], [10]. On average, the resolution is around 25 m. The images were rectified to a Finnish Uniform Coordinate System (northing and easting in meters) with a 25-m pixel spacing, and thus, the correlation between neighboring pixels is now negligible. The noise equivalent σ° is below -22 dB [9], [10].

III. ANALYSIS METHODS OF SPATIAL STATISTICS

First, we would like to recall the expression for the sample variance of n -correlated measurement X_i with the same finite variance σ^2 . The expectation of the sample variance can be

computed using only the definition of variance for the sum of random variables and then rearrangement of terms. The result is (e.g., see [11])

$$E(s^2) = E\left(\frac{\sum_{i=1}^n (X_i - \bar{X})^2}{n-1}\right) = \sigma^2 \left(1 - \frac{\delta_n(\rho)}{n-1}\right) \quad (1)$$

where the bias term is the sum of the pairwise correlations

$$\delta_n(\rho) = \frac{1}{n} \sum_{i \neq j} \rho(i, j).$$

If the correlations between measurements near each other are positive and far apart decrease to zero, the bias term in (1) becomes negligible when the measurement length is long enough. In these situations, the sample variance increases with increasing measurement length even in the stationary case, the exact form of increase depending on the prevailing correlation structure.

For reasons outlined in Section I, we are particularly interested in finding out whether the standard deviations (stds) of the σ° values measured along a line exhibit the same kind of statistical dependence on the measurement length as is characteristic of fractal-like profiles, like samples from a self-similar nonstationary fractional Brownian profile. The continuous self-similar Gaussian process $B_H(t)$, indexed by a Hurst parameter H ($0 < H < 1$), which has the fractional Gaussian noise (fGn) as its stationary increment process, is called fractional Brownian motion (fBm) (e.g., see [11]). Due to Gaussianity, the process $B_H(t)$ is fully specified by the expected value and the covariances.

The functional dependence of the std σ of an fBm on the measurement length l has a power-law form [12]

$$\ln(\sigma) = a + b \ln(l). \quad (2)$$

The coefficient a is related to the actual profile level, whereas b describes the variation of the profile with spatial frequency.

The b coefficient is related to the fractal dimension D as

$$b = 2 - D. \quad (3)$$

Another way to formulate the dependence in question is to consider the stds of increments of an fBm profile (Allan std) [13]. Then it holds

$$\text{std}[z(x + \Delta x) - z(x)] = c\Delta x^b. \quad (4)$$

In this study, we investigated only the dependence between $\ln(l)$ and $\ln(\text{std}(\sigma^\circ))$ as $\text{std}(\sigma^\circ)$ has been traditionally used in σ° data analysis and classification. Additionally, the dependence of (2) has been investigated for the Baltic Sea ice surface profile data [1].

Based on the value of the Hurst parameter H , the corresponding fBm can be classified into three different categories [11]. If $H \in (1/2, 1)$, then the associated increment process fGn is long-range dependent (positive correlation between increments far apart); if $H = 1/2$, the associated increment process consists of independent identically distributed (i.i.d.) normal variables (the ordinary Brownian motion); and if $H \in (0, 1/2)$, the increment process shows only short-range dependence (negative correlation between two successive increments). The

different correlation structures of the increment processes result in different growing rates of σ as a function of l . In our notation, the parameter b in (2) equals H .

In the following, the calculation method of (2) for discrete profiles is first discussed, and then, using simulated fractal and single-scale autocorrelation function (ACF) profiles, we examine the accuracy of our calculation method and what kind of results one can expect if σ° follows either fractal, single-scale ACF, or random process i.i.d. variables. Finally, the calculation of (2) for HUTSCAT and ENVISAT data is described.

A. Calculation Method for General Discrete Profiles

The std σ as a function of length l is calculated in the following steps.

- Step 1) A profile is divided into disjoint segments with a fixed length giving n segments per profile. The value of n depends on the profile length.
- Step 2) A window of length d is slid through a segment by one-pixel steps. In every allowed window position σ is computed. This yields m distinct σ values for every segment.
- Step 3) m values of σ are averaged for each segment separately.
- Step 4) Steps 2) and 3) are repeated when d increases from the minimum to the maximum length.
- Step 5) For each segment, (2) is fit using d as the explaining variable. This yields n sets of regression coefficients for each profile.

The calculation process explained above also illuminates a property associated to this approach. The regression coefficient b in (2) yields information on how large-scale and small-scale variations occur in a given segment. On the other hand, this information cannot be extracted from σ or ACF statistics because they are calculated only at one fixed length. Hence, if the fractal-like property holds, the proposed approach would give us new information about the nature of the local oscillation structure of signal statistics.

B. Accuracy of the Analysis Method

Due to their inherent nature, fractals are analyzed by multi-scale methods, e.g., box counting method and wavelet analysis [14]. For image data, local fractal dimension (LFD) has been used as a feature in texture classification in many studies (e.g., [15]–[17]). Typically, LFD is estimated in windows around each data pixel. Usually, suitable window sizes for estimating LFD are defined experimentally as compromises between desired classification resolution and precision of the estimates. In several studies, comparisons of the estimates to fractal signals (images) with known fractal dimension have been made, and it seems that the estimates are typically not very accurate, like e.g., in [15].

In our approach, a large set of estimates for a fractal dimension D with (3) is first calculated using only a limited data set (segments) and then the global D estimate is obtained by averaging over these local dimension estimates. To examine the accuracy level of the D estimates obtained with the proposed calculation method, its behavior is studied in three disparate cases using simulated data sets. The first data set consists of simulated fBm profiles, while the second data set consists

TABLE II
AVERAGE ESTIMATED FRACTAL DIMENSION D AND COEFFICIENT OF DETERMINATION FOR fBm PROFILES WITHOUT FADING

Theor. D	Fracla b	Overlapping windows			Disjoint windows		
		Full profile	Segment $n=60$	Segment $n=40$	Segment $n=20$	Full profile	Segment $n=40$
1.9	1.97	1.89 0.94	1.89 0.91	1.89 0.86	1.90 0.76	1.91 0.77	1.89 0.29
1.7	1.72	1.74 0.97	1.75 0.97	1.76 0.93	1.77 0.88	1.73 0.91	1.78 0.36
1.5	1.54	1.57 0.97	1.59 0.97	1.60 0.96	1.65 0.93	1.55 0.90	1.65 0.44
1.3	1.32	1.38 0.99	1.43 0.98	1.45 0.98	1.48 0.97	1.34 0.94	1.51 0.51
1.1	1.12	1.13 0.99	1.28 0.99	1.29 0.99	1.33 0.99	1.13 0.98	1.37 0.64
SSE ¹⁾	0.008	0.014	0.058	0.072	0.114	0.006	0.146

1) SSE = the sum of squares of the errors

of some single-scale Gaussian and exponential ACF profiles. Such profiles are of interest because they exhibit functional dependence between σ and l if the profile length is relatively short with respect to the profile correlation length. Finally, the method was applied for a random process with i.i.d. variables, where σ will saturate quickly as a function of l . In all cases, our main interest was to see if the calculation method can reveal the nature of dependence of σ on l .

We simulated fBm profiles with H values of 0.1, 0.3, 0.5, 0.7, and 0.9. At each H value, ten profiles of length 1024 points were simulated. The simulations were performed using the Fraclab software, which is a freeware fractal analysis Matlab toolbox [18]. The length of the single-scale Gaussian and exponential ACF was set to 1000 points. Their std was fixed to five points and profile correlation length had values of 5, 50, and 100. Ten profiles were simulated at each correlation length value. The i.i.d. profiles were also 1000 points in length.

Before the analysis, the minimum and maximum length for d in Step 4) must be chosen. The minimum length d_{\min} was chosen to be five profile points. When d increases, the amount of sample estimates of σ decreases and their average is subject to greater random variation. The choice for the maximum length d_{\max} depends on how much random variation is allowed. In [19], the maximum length was chosen empirically to be 60% of the segment length. Here, this limit and also lengths of 40% and 50% are tested to see how the value of b coefficient and the model fitting accuracy (coefficient of determination r^2 for regression) behave as a function of d_{\max} . The results are used to determine d_{\max} for all data analyses.

The fractal dimension D of the profiles is estimated using both full-length profiles and separate segments of length of 20, 40, and 60 points. Segmentwise analysis emulates our analysis of radar data, where a segment length of 40 points will be used. It produces a large number of D estimates for a single profile. These estimates are all averaged together. In case of fBm profiles, the D estimates with (3) are compared to those obtained with the Fraclab (calculates regularization dimension [20]). The results for the fBm and single-scale exponential ACF profiles when d_{\max} is 60% of the segment length are shown in Tables II and III, respectively.

Equation (3) always gives an accurate estimate for the fractal dimension D of the full-length fBm profile (max error of 0.08

TABLE III
AVERAGE ESTIMATED FRACTAL DIMENSION D AND COEFFICIENT OF DETERMINATION FOR SINGLE -SCALE EXPONENTIAL ACF PROFILES. FADING IS CHARACTERIZED BY 50 INDEPENDENT SAMPLES

rms height	corr. length	Full profile without fading	Segment n=40 without fading	Full profile with fading	Segment n=40 with fading
5	10	1.90 0.74	1.67 0.96	1.93 0.75	1.79 0.92
5	50	1.74 0.93	1.60 0.97	1.82 0.96	1.82 0.91
5	100	1.66 0.97	1.59 0.97	1.77 0.98	1.83 0.89

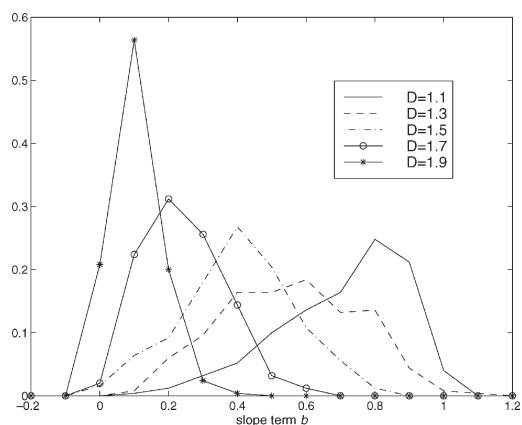


Fig. 1. PDFs for the slope term b of (2) estimated from the 40-point segments of ten fBm profiles with theoretical D from 1.1 to 1.9. The bin width is 0.1 in the pdfs. Number of b coefficients at each D value is 250.

when compared to Fraclab results). When the maximum length decreases from 60% to 50% and further to 40%, the accuracy of the estimated D on the average increases slightly. However, this increase is so small that the maximum length of 60% used in [19] can also be used very well in here.

With the short segments of the fBm profile, the accuracy of D estimation decreases. A segment length of 20 points yields with (3) estimates of D that are close to the theoretical one only when $D \geq 1.7$. For segments of 40 and 60 points, a good correspondence also exists when $D = 1.5$. For (2), r^2 is very high at all theoretical D values when the segment length is either 40 or 60 points. These results indicate that a segment of 40 points is long enough for the accurate detection of a linear relationship between $\ln(l)$ and $\ln(\sigma)$.

When a window of length d is slid through a profile or a short segment by one point steps, the obtained consecutive σ values are not computed from disjoint data sets. To see whether this has an effect on the results, the window was also slid by steps equal to its length. The D estimates obtained this way are very close to those estimated with the window sliding by one point step; the absolute difference is at maximum only at 0.08 (see Table II). However, r^2 is now clearly smaller. The smaller r^2 is due to the small number of individual σ estimates available at longer measurement lengths for averaging, yielding more variable $\ln(l)$ versus $\ln(\sigma)$ curves.

The magnitude of variation of the b coefficient for a segment length of 40 points is studied using the probability density functions (pdfs) shown in Fig. 1. These distributions are based

on the simulated fBm realizations. The pdfs at different values of D have a very wide support and overlap with each other. On the basis of Fig. 1, it is evident that one cannot expect accurate separation between fBm profiles, which have different values of D , using only a single b value computed from a short segment. On the other hand, the encouraging features seen in Fig. 1 are that the empirical mean values and modes of the b parameters preserve the theoretically correct ordering as a function of D . Hence, a single b value is a meaningful discriminant. A coarse separation utilizing only a single b value is possible, e.g., the fBm profiles with D close to 1 can be separated in most cases from profiles with D close to 2. Even if sea ice radar data would follow the fBm behavior, it would not be possible to identify various ice-type classes based on the b coefficient of a short segment. However, a coarse classification like SLI versus HDI could be possible.

For the single-scale ACF profiles, the estimated D decreases when the correlation length increases, i.e., when a profile becomes smoother. For an exponential profile, the estimated D is larger than for a Gaussian profile as the exponential profile is locally rougher. When the correlation length is short, e.g., 10 points, σ saturates well before the 60% length is reached, and this results in a low r^2 . However, with increasing correlation length, the statistics are very similar to those of an fBm. When the profile length is increased, r^2 starts to decrease, indicating poor support for the assumption of the linear dependence between $\ln(\sigma)$ and $\ln(l)$, as is the case. With short segments, the estimated D is approximately equal for all three different values of the profile correlation length. The average r^2 for (2) is always very high.

For short segments of i.i.d. profiles, the estimated D is very close to 2, e.g., for random fading with 50 independent samples, the average b for segments of 40 and 20 points is around 0.02 and 0.03, respectively. The linear dependence between $\ln(\sigma)$ and $\ln(l)$ is practically nonexistent.

We conclude that our analysis method can reliably detect whether σ in the short profile segment increases with increasing l according to (2) if this is theoretically the case. There exist nonfractal profiles that on short intervals exhibit the same kind of power-law dependence between σ and l as a fractal realization. Hence, by utilizing only short segments of profile data, it is not possible to determine if the profile is truly fractal like, i.e., to determine if σ obeys some power law as a function of l .

C. Effect of Fading

The fading was added to the profiles according to the following model for the radar intensity I [21], i.e.,

$$I = \mu_I \cdot T \cdot F_N \quad (5)$$

where

- μ_I mean intensity;
- T texture random variable that represents the natural spatial variability of the intensity, $E[T] = 1$;
- F_N fading random variable characterized by a normalized χ^2 distribution with $2N$ degrees of freedom (N is the number on independent samples), $E[F_N] = 1$, $\text{Var}(F_N) = 1/N$.

TABLE IV
AVERAGE ESTIMATED FRACTAL DIMENSION D AND COEFFICIENT
OF DETERMINATION FOR fBm PROFILES WITH FADING
CHARACTERIZED BY 50 INDEPENDENT SAMPLES

Theor. D	Fraclab	Full profile	Segment $n=40$
1.9	1.99	1.92 0.92	1.92 0.82
1.7	1.83	1.83 0.97	1.88 0.88
1.5	1.76	1.74 0.95	1.87 0.85
1.3	1.66	1.68 0.95	1.88 0.83
1.1	1.71	1.64 0.88	1.92 0.75
SSE	0.60	0.51	1.18

The texture variable T is modeled as a trajectory of the fBm or a single-scale exponential ACF profile. The number of independent samples N was chosen to be 10 and 50. The first figure is a rough estimate for the ENVISAT IMP data rectified to a pixel size of 25 m, and the second one for the HUTSCAT data at a resolution of 12.5 m. Before adding fading to the profiles, their minimum value was moved to 0.001 (i.e., -30 dB) to avoid negative intensity values. The profile mean was set to 1.

When fading is added to the fBm profiles, the estimated D is still increasing monotonously with the increasing theoretical D , but small D values are greatly overestimated, i.e., the range of D estimates is decreased (see Table IV). This is due to the fading that adds fast local variations to the fBm profiles and thus makes them locally considerably rougher than the original profiles. The average r^2 for (2) is always high.

With the fBm profile segments, the estimated D is now approximately equal regardless of the theoretical D . Consequently, it is not possible to obtain even a coarse estimate of the true D using short segments. The linear dependence between $\ln(l)$ and $\ln(\sigma)$ is still moderately present. The pdfs for b with different theoretical D are now very wide and totally mixed with each other, making classification of the segments based on a single b value impossible. However, the average b values are clearly larger than the average b of 0.02 for random fading (i.i.d. case).

In general, if the textural variation of the sea ice σ° follows the fBm behavior, then the proposed analysis method, using small segments of the measured σ° data, would yield a quite constant slope term b regardless of D for the target (i.e., ice type) σ° texture and, thus, very poor classification of ice types. However, the average b would be clearly larger than that for an i.i.d. process (e.g., random fading). The linearity between $\ln(\sigma)$ and $\ln(l)$ would be moderate. Whereas if the σ° texture follows the behavior of a profile with Gaussian or exponential ACF, then short segments would yield average b with only a small range of values as a function of texture correlation length (see Table III). The average b would again be larger than for the i.i.d. process. The linearity between $\ln(\sigma)$ and $\ln(l)$ would be from moderate to quite strong. Finally, if the variation of the measured sea ice σ° data is an i.i.d. process, then within the small segments the linearity between $\ln(\sigma)$ and $\ln(l)$ would be very weak and the average b very close to zero.

TABLE V
STATISTICS FOR THE COEFFICIENT OF DETERMINATION r^2 AND
REGRESSION COEFFICIENT b OF (2) USING 5.4-GHz HH-POLARIZATION
HUTSCAT SCATTEROMETER DATA ACQUIRED AT AN INCIDENCE
ANGLE OF 23° UNDER DRY SNOW CONDITIONS

	NI	SLI	RLI	SDI	HDI	FBI
Data amount	13	29	21	27	105	19
Average r^2	0.89	0.84	0.82	0.92	0.83	0.79
std r^2	0.15	0.19	0.27	0.08	0.23	0.25
Average b	0.150	0.118	0.147	0.177	0.141	0.093
std b	0.107	0.113	0.155	0.113	0.100	0.083

D. Analysis of HUTSCAT and ENVISAT Data

First, the HUTSCAT data were averaged to a resolution of 12.5 m that compares to the pixel size of many spaceborne SAR images. The averaged data have around 50 independent samples in each σ° . The std of fading is then below 0.62 dB. The segment length in (2) was chosen to be 40 consecutive σ° values, which corresponds to the measurement length of 487.5 m. The chosen segment length is a compromise between a long segment for a large number of points in (2) and a short segment applicable for informative classification. The number of segments for an ice type varies from 4 to 105.

Rectangular areas representing LI, DI, and HDI were visually selected from each ENVISAT SAR image. As the visual discrimination between RLI and SDI in the SAR images is difficult, these two HUTSCAT ice-type classes were combined as one DI-type class. The LI class corresponds to SLI in the HUTSCAT data. The HDI class is a mixture of SDI and HDI classes of the HUTSCAT data. NIs were not present in the SAR images. A typical area of a rectangle was 15 km². Within each rectangle, ten windows of size 40 \times 40 pixels (1000 \times 1000 m) were selected at random locations. The average number of windows for each ice type is around 140. Equation (2) was calculated as in the case of the HUTSCAT data, but the average σ was calculated separately for horizontal and vertical directions and then these two estimates were averaged together as no noticeable anisotropy was detected. For the ENVISAT data, the segment length of 40 σ° values corresponds to a measurement length of 975 m.

IV. RESULTS AND DISCUSSION

The linear relationship between $\ln(\text{std}(\sigma^\circ))$ and $\ln(l)$ is studied separately with the HUTSCAT and ENVISAT data as the HUTSCAT data have been reliably divided into a total of seven different ice classes using video imagery, whereas it was feasible to classify the ENVISAT data to only three ice types. However, the ENVISAT results are compared to HUTSCAT ones. The ice-type classification capability of the regression coefficients in (2) is compared to the mean and std of σ° in the decibel scale.

A. HUTSCAT Data

A clear linear dependence between $\ln(l)$ and $\ln(\text{std}(\sigma^\circ))$ was observed in the HUTSCAT data. The average r^2 for all data is 0.84, and only 23% of the total of 3096 segments is r^2 below 0.80. The fluctuation of r^2 does not exhibit dependence on

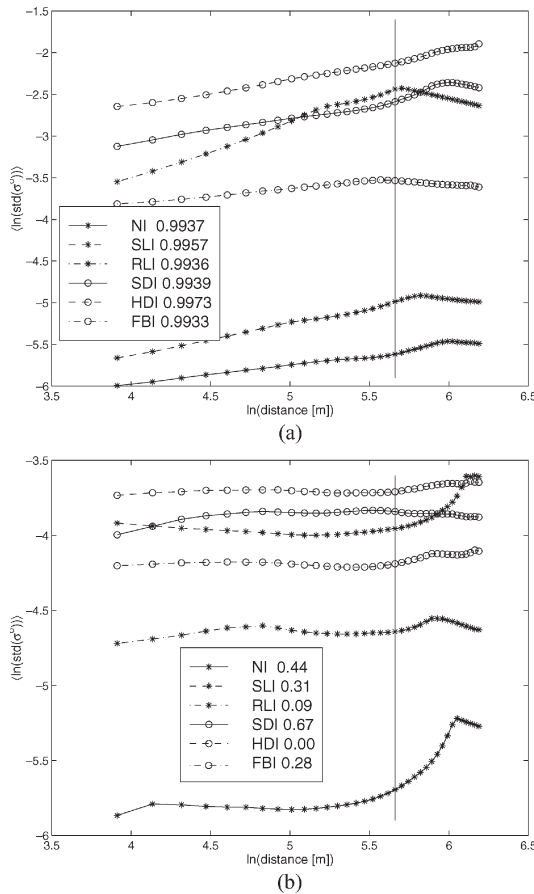


Fig. 2. (a) Strongest and (b) weakest dependence between $\ln(l)$ and $\ln(\text{std}(\sigma^\circ))$ for various ice types using HUTSCAT 5.4-GHz HH-polarization dry snow Baltic Sea ice data. The section length is 40 σ° values (distance of 487.5 m). The incidence angle is 23°, and the data were averaged to a resolution of 12.5 m. The maximum and minimum coefficients of determination for each ice type are given. The vertical line shows the maximum distance used in (2) according to the 60% rule.

snow condition, polarization, or incidence angle. An example statistics for r^2 and b are presented in Table V. The dependence between $\ln(l)$ and $\ln(\text{std}(\sigma^\circ))$ for those segments of 40 pixels where r^2 has its maximum or minimum value for each ice type is shown in Fig. 2 at 5.4-GHz HH-polarization. To see whether the linear relationship between $\ln(l)$ and $\ln(\text{std}(\sigma^\circ))$ extends to longer segment lengths, the measurement lines of various ice types were used in their full length (max 60% length 6.5 km, average 650 m) in the analysis. The average r^2 is still high (0.84), and there is no correlation between r^2 and the length of measurement line. This suggests the increase of $\text{std}(\sigma^\circ)$ as a function of l up to a distance of at least a few kilometers.

The statistical confidence of the obtained segmentwise b values was estimated using the variation coefficient (vc) of $\text{std}(\sigma^\circ)$ and applying t-test to hypothesis testing: $H_0: b = 0$; $H_1: b > 0$; risk level 0.05. The average vc for windows of length from 5 to 24 pixels (24 is the 60% length) is typically around 0.65 at the minimum length and then decreases exponentially to around 0.20 at maximum length. The hypothesis H_0 is rejected for 92% of the total b values. Hence, on the basis of these results, we conclude that: 1) the obtained b values mostly have high statistical confidence; 2) b values are not considerably influenced by limited sample sizes for average $\text{std}(\sigma^\circ)$; and

3) the large stds of b shown in Table V are due to the large statistical variability of the individual segments.

When comparing HUTSCAT results with the simulated ones in Section III-C, it seems that σ° as a function of l for sea ice cannot completely be described either by the fractal, single-scale ACF, or random process of i.i.d. variables. The dependence of σ° versus l is likely a more complicated process, e.g., a multi-fBm with a spectrum of different kinds of singularities [22].

The average b is usually the largest for SDI (from 0.094 to 0.250) and the smallest for FBI (from 0.067 to 0.174). These averages are clearly larger than the values obtained for profiles of random fading (i.i.d. process). In case of an fBm profile, the smaller b is, the more uniformly and densely distributed are the significant changes in the profile. FBI is very homogeneous in its surface structure, and thus its σ° has most likely small textural variations without any large-scale (i.e., low spatial frequency variation) patterns, which results in a small b value. Whereas in the case of SDI, the overall level of σ° intensity may remain low (or high) on a relatively long interval before a large jump. The large-scale variation for SDI induced by the ridging intensity variation is greater than the local variation due to the small-scale texture and the fading. This property is reflected in the large b . The structure of HDI also exhibits a variation between ridged ice and LI as SDI, but the fraction of DI is consistently high, and thus, the large-scale variation of σ° is smaller than for SDI.

There are no systematic differences on the average segmentwise b values between HH- and VV-polarizations. Under all snow conditions, the average b at cross-polarization for SDI, HDI, and FBI is consistently larger, on the average by 33%, than at copolarizations. At cross-polarization, the σ° contrast between LI and DI is larger than at copolarizations [23], yielding increased large-scale textural variation of σ° . For other ice types, both increasing and decreasing trends exist.

When the incidence angle increases from 23° to 45°, the average b at copolarizations for SDI and HDI increases on average by 30%. At cross-polarization, both increasing and decreasing trends exist. For LI areas in a DI field, the magnitude of decrease of σ° with increasing incidence angle is larger than for DI areas, which produces more pronounced large-scale variation of σ° at an angle of 45° [24]. At copolarizations, the decrease of σ° with increasing incidence angle is larger than at cross-polarization [23]. For NI and LI types, no consistent trends for b exist.

Under the dry snow condition, the average b for SDI and HDI is always somewhat larger (on the average 10%) than under moist snow conditions. For FBI, on the contrary, the trend is always opposite (average 43%). This is also mostly the case for NI and RLI (average decrease 27%). When the snow cover is wet, the average b is always the smallest and the relative difference to dry snow condition is around 75%. In case of DI types, the observations can be explained by the effect of the snow cover wetness, which diminishes or even prevents backscattering from underlying the sea ice surface. The surface of the snow cover is usually smoother than that of sea ice [1]. The increasing trend from dry to moist snow condition can also be due to random fluctuation, at least partly, as the data sets

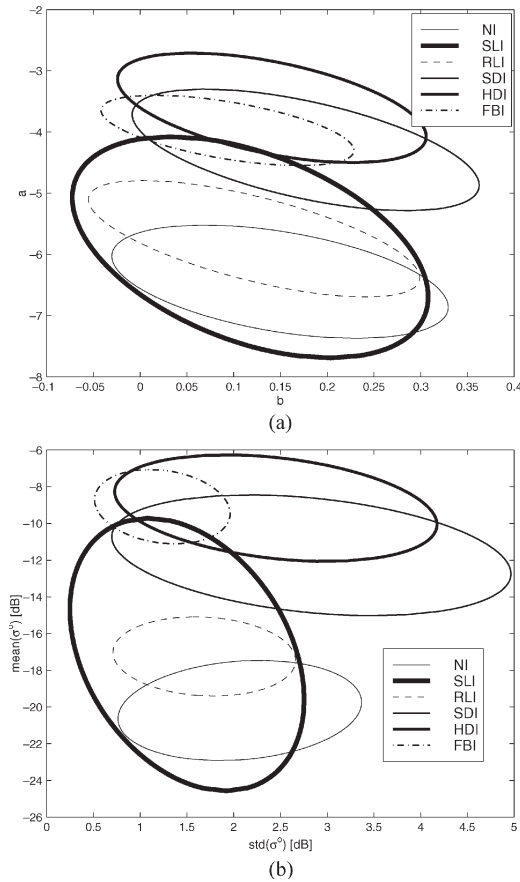


Fig. 3. Variation of (a) regression coefficients a and b of (2) and (b) mean and std for a section of $40 \sigma^\circ$ values (distance of 487.5 m) of various ice types using HUTSCAT 5.4-GHz HH-polarization dry snow Baltic Sea ice data. The incidence angle is 23° , and the data were averaged to a resolution of 12.5 m. Ellipses represent 90% confidence limits.

of the three snow conditions were acquired from different ice fields. The effect of snow cover should be studied by measuring the same ice field under various snow wetness conditions. This can be done with the ENVISAT data.

When the data resolution decreases, textural variations of σ° are more and more averaged, but the effect of fading is reducing faster. The net effect is that in the total variation of σ° the large-scale oscillations become more pronounced. The decrease of resolution should therefore increase the average b (up to some resolution limit). The effect of resolution was studied by calculating average b values also at a resolution of 25 m for a distance of 487.5 m. When the resolution decreases from 12.5 to 25 m, the average b increases in almost all cases. The increase is the smallest for SDI and HDI (average 13%) and the largest for SLI and FBI (average 56%). The textural variations in SLI and FBI are smaller than in other ice types, and when fading reduces they become more visible.

The distribution of the b and a values is so large that unambiguous ice-type discrimination is not possible in any snow condition, which is understandable as the ice roughness variation and, thus, also the σ° variation constitute a continuum instead of distinctly separable classes [1]. On the basis of Fig. 3, the DI types (HDI, SDI, FBI) are as well separated from LI areas as by using only the mean and std of σ° . According to our assessment, both methods perform equally well for this

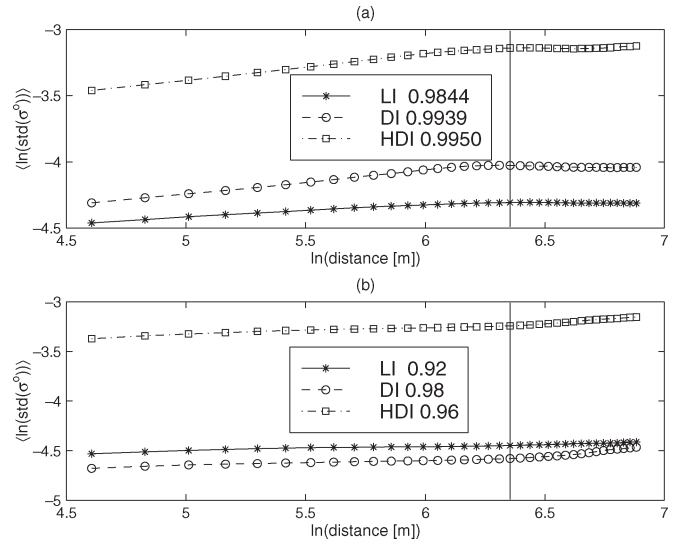


Fig. 4. (a) Strongest and (b) weakest dependence between $\ln(l)$ and $\ln(\text{std}(\sigma^\circ))$ for three ice types using ENVISAT HH-polarization data acquired over the northern part of the Bay of Bothnia in February 15, 2003. The section length is $40 \sigma^\circ$ values (distance of 975 m). The pixel size in the ENVISAT data is 25 m. The maximum and minimum coefficients of determination for each ice type are given. The vertical line shows the maximum distance used in (2) according to the 60% rule.

data set when the window size is relatively large (40 pixels). The disadvantage of using the std values is that they are fixed for a certain distance. The results of our analysis support an assumption that there exists two types of uncertainties in the estimation of std for σ° data. In addition to the uncertainty due to sampling size, the value of std also seems to depend on the measurement length. Hence, an accurate comparison with corresponding values of different studies does not seem to be possible if the distance used for their determination is not equal.

B. ENVISAT Data

The average r^2 for all data is very high (0.98), and only 6.2% of the total of 2460 r^2 values is below 0.95. The average r^2 is larger than in the HUTSCAT data, most likely due to the very large amount of distinct $\text{std}(\sigma^\circ)$ values available for averaging in the ENVISAT data. An example of the dependence between $\ln(l)$ and $\ln(\text{std}(\sigma^\circ))$ for the ENVISAT data is shown in Fig. 4. For LI, DI, and HDI, the average b varies from 0.058 to 0.144 (see Table VI). These averages are larger than those of around 0.03 for random i.i.d. processes. The statistical confidence of the obtained b values is high as the hypothesis, $H_0: b = 0$; $H_1: b > 0$, is always rejected with risk level 0.05, and the vc of $\text{std}(\sigma^\circ)$ is on average around 0.6 at minimum length and decreases to 0.3 at maximum length. The vc of b for each ice type varies from 0.13 to 0.34. For the HUTSCAT data, it is from 0.52 to 1.14. This difference between the data sets is likely due to the different ice-type definitions, data resolutions, and number of $\text{std}(\sigma^\circ)$ values for averaging.

The average b always increases with increasing ice deformation (89% on the average). At HV-polarization, the average b for HDI is always slightly larger (23% on the average) than at HH-polarization. For the other two ice types, there are both small increasing and decreasing trends. The effect of incidence angle was studied using the SAR images acquired on February 14

TABLE VI
STATISTICS FOR THE REGRESSION COEFFICIENT b OF (2) USING ENVISAT SAR DATA ACQUIRED IN THE BAY OF BOTHNIA IN FEBRUARY 2003

Date	Image Swath	Polarization	Inc. Angle	Snow Cover	Data Amount			Average b			Std b		
					LI	DI	LI	LI	DI	HDI	LI	DI	HDI
14 Feb	IMP IS3	HH	28.6-30.9	Dry	140	140	130	0.058	0.107	0.113	0.010	0.037	0.025
15 Feb	APP IS6	HH HV	39.1-42.6	Dry	110	150	150	0.061 0.066	0.100 0.090	0.122 0.144	0.010 0.008	0.025 0.025	0.025 0.037
16 Feb	IMP IS1	HH	15.3-20.5	Moist	110	150	150	0.060	0.087	0.103	0.011	0.022	0.024
19 Feb	APP IS2	HH HV	19.6-24.7	Dry	110	150	150	0.070 0.074	0.099 0.094	0.111 0.142	0.010 0.016	0.023 0.027	0.024 0.040

and 15 under similar snow and weather conditions. When the incidence angle increases from 28.6°–30.9° (on February 14) to 39.1°–42.6° (on February 15), the average b for LI and HDI at HH-polarization slightly increases (around 7%), but for DI it slightly decreases (around 7%). DI is a mixture of RLI and SDI ice types for the HUTSCAT data; for SDI, an increase of b with increasing incidence angle was always observed, but for RLI b sometimes decreased.

The effect of snow wetness condition was studied with the SAR images on February 16 and 19. Unlike the case of HUTSCAT data, these images were acquired over the same ice field. Under the dry snow condition, the average b at HH-polarization is always a little larger (on the average 13%) than under the moist snow condition. This result confirms the speculated reason for the decrease of the average b with increasing snow wetness in the HUTSCAT data: a moist snow cover reduces the large-scale textural variation of σ° as it either prevents or considerably attenuates scattering from sea ice.

Equation (2) was also studied using a window of size 80×80 pixels (2000×2000 m) for the SAR image of February 15. The average r^2 decreases only slightly when the window size increases; at HH-polarization, the average r^2 is 0.98 and 0.96 at window sizes of 1000 and 2000 m, respectively. The average b for LI and HDI decreased on the average by 26% and 19%, respectively. This decrease could indicate that the dependence of σ° is changing as a function of spatial frequency.

A typical increase of $\text{std}(\sigma^\circ)$ in decibel scale with increasing $N \times N$ window size was investigated using the ENVISAT image acquired on February 14. The average $\text{std}(\sigma^\circ)$ for LI increased from 1.87 dB for a 5×5 window to 1.96 dB for a 20×20 window. For HDI, the corresponding figures are 2.34 and 2.73 dB. For LI, the increase is subtle, but for DI types it is noticeable.

In general, the ENVISAT results and their explanations are identical to the HUTSCAT ones. The differences are likely due to the different number of independent samples and different ice-type definitions for the HUTSCAT and ENVISAT data. The discrimination capability of the coefficient pair (a, b) is comparable to that of the mean and std of σ° when the window size is 1000 m. Because the data analysis results indicate a dependence of $\text{std}(\sigma^\circ)$ of the measurement length, one could utilize this property, e.g., by designing a classifier that uses multiple different window sizes as a feature vector.

V. CONCLUSION

We have studied the dependence between measurement length l and std for the Baltic Sea ice σ° using C-band

HUTSCAT scatterometer data and ENVISAT ASAR IMP and APP images. The results with both data sets indicate in almost all cases an increase of $\text{std}(\sigma^\circ)$ with increasing l . In addition, there is mostly a very good linear relationship between $\ln(l)$ and $\ln(\text{std}(\sigma^\circ))$ up to a distance of at least a few kilometers. This dependence is described by the slope term b of (2), which for fBm profiles is related to the fractal dimension $D = 2 - b$. It was found that the average b depends on ice type, polarization, incidence angle, snow cover wetness, and data resolution if the number of independent samples also changes.

The linear dependence between $\ln(l)$ and $\ln(\text{std}(\sigma^\circ))$ is a property of fBm, but within short data segments this property is also valid for some nonfractal profiles. Based on our analysis of empirical and simulated data, it seems that sea ice σ° as a function of l is not completely described by either the fractal, single-scale ACF, or random process of i.i.d. variables. The dependence of σ° versus l is likely a more complicated process, e.g., a multi-fBm.

The scatter in the values for coefficients b and a is so large that unambiguous ice-type discrimination is not possible using either one of them alone or both together. In our data set, DI types were mostly discriminated from other ice types, but this discrimination was not essentially better than that obtained with just the mean and std of σ° determined for the same window size as b and a . It is possible that a relation exists between b computed from the surface profile of large-scale sea ice deformation [i.e., the slope term for $\ln(l)$ versus $\ln(\text{std}(\text{surface height}))$] and b computed from the σ° profile. This assumption could only be studied with quantitative ground truth data describing ice surface topography. The use of parameters b and a instead of std and mean is preferred due to the scale-invariant comparability with the results of other studies obtained with different calculation window sizes and with radar instruments of different resolutions. As there is dependence of $\text{std}(\sigma^\circ)$ on l , this should be taken into account in the data analysis, e.g., when constructing classifiers for sea ice SAR data. One way to utilize this property is to design a classifier that uses multiple different window sizes as a feature vector.

REFERENCES

- [1] A. T. Manninen, "Surface roughness of Baltic Sea ice," *J. Geophys. Res.*, vol. 102, no. C1, pp. 1119–1139, Jan. 1997.
- [2] O. I. Yordanov and A. Guissaird, "Approximate self-affine model for cultivated soil roughness," *Physica A*, vol. 238, no. 1–4, pp. 49–65, Apr. 1997.
- [3] M. W. J. Davidson, T. Le Toan, F. Mattia, G. Satalino, T. Manninen, and M. Borgeaud, "On the characterization of agricultural soil roughness for radar remote sensing studies," *IEEE Trans. Geosci. Remote Sens.*, vol. 38, no. 2, pp. 630–640, Mar. 2000.
- [4] A. T. Manninen and L. M. H. Ulander, "Forestry parameter retrieval from texture in CARABAS VHF-band SAR images," *IEEE Trans. Geosci. Remote Sens.*, vol. 39, no. 12, pp. 2622–2633, Dec. 2001.
- [5] F. Berizzi and E. Dalle-Mese, "Scattering from a 2-D sea fractal surface: Fractal analysis of the scattered signal," *IEEE Trans. Antennas Propag.*, vol. 50, no. 7, pp. 912–925, Jul. 2002.
- [6] M. Hallikainen, J. Hyypä, J. Haapanen, T. Tares, P. Ahola, J. Pulliainen, and M. Toikka, "A helicopter-borne eight-channel ranging scatterometer for remote sensing—Part I: System description," *IEEE Trans. Geosci. Remote Sens.*, vol. 31, no. 1, pp. 161–169, Jan. 1993.
- [7] A. Seinä, H. Grönvall, S. Kalliosaari, J. Vainio, P. Eriksson, and J.-E. Lundqvist, "WMO sea ice nomenclature: Terminology for the Baltic Sea in English, Finnish and Swedish," Finnish Marine Res. Inst., Helsinki, MERI Rep. 43, 2001.

- [8] M. Hallikainen, F. T. Ulaby, and M. Abdelrazik, "Dielectric properties of snow in the 3 to 37 GHz range," *IEEE Trans. Antennas Propag.*, vol. AP-34, no. 11, pp. 1329–1340, Nov. 1986.
- [9] P. J. Meadows and P. A. Wraith, "ASAR image mode product quality," in *Proc. IGARSS*, Toulouse, France, 2003, pp. 1112–1114.
- [10] P. Meadows and P. Wraith, "ASAR APP and APM image quality," presented at the Proc. ENVISAT Validation Workshop, Frascati, Italy, Dec. 9–13, 2002, Paper ESA SP-531.
- [11] J. Beran, *Statistics for Long-Memory Processes*. London, U.K.: Chapman & Hall, 1994.
- [12] E. L. Church, "Fractal surface finish," *Appl. Opt.*, vol. 27, no. 8, pp. 1518–1526, Apr. 1988.
- [13] J. M. Keller, R. M. Crownover, and R. Y. Chen, "Characteristics of natural scenes related to the fractal dimension," *IEEE Trans. Pattern Anal. Mach. Intell.*, vol. PAMI-9, no. 5, pp. 621–627, Sep. 1987.
- [14] S. Mallat, "A theory for multiresolution signal decomposition: The wavelet representation," *IEEE Trans. Pattern Anal. Mach. Intell.*, vol. 11, no. 7, pp. 674–693, Jul. 1989.
- [15] S. S. Chen, J. M. Keller, and R. M. Crownover, "On the calculation of fractal features from images," *IEEE Trans. Pattern Anal. Mach. Intell.*, vol. 15, no. 10, pp. 1087–1090, Oct. 1993.
- [16] M. Gambini, M. Mejail, J. Jacobo, and C. Delrieux, "SAR image segmentation through B-spline deformable contours and fractal dimension," in *Proc. ISPRS*, Istanbul, Turkey, 2004.
- [17] H. T. Ewe, H. K. Low, and H. T. Chuah, "Fractal surface dimension for classification of remotely sensed data," in *Proc. 18th Asian Conf. Remote Sens.*, Kuala Lumpur, Malaysia, 1997, pp. I-5-1–I-5-6.
- [18] *FracLab: A Fractal Analysis Toolbox for Signal and Image Processing*, INRIA—The French Nat. Inst. Res. Comput. Sci. and Control. [Online]. Available: <http://complex.inria.fr>
- [19] A. T. Manninen, "Multiscale surface roughness description for scattering modelling of bare soil," *Physica A*, vol. 319, no. 1, pp. 535–551, Mar. 1, 2003.
- [20] F. Roueff and J. Lévy Véhel, "A regularization approach to fractional dimension estimation," in *Proc. Fractal—Fractals and Beyond*, M. M. Novak, Ed. Singapore: World Scientific, 1998.
- [21] F. T. Ulaby, F. Kouyate, B. Brisco, and T. H. L. Williams, "Textural information in SAR images," *IEEE Trans. Geosci. Remote Sens.*, vol. GRE-24, no. 2, pp. 235–245, Mar. 1986.
- [22] S. Jaffard, Y. Meyer, and R. D. Ryan, *Wavelets. Tools for Science and Technology*. Philadelphia, PA: SIAM, 2001.
- [23] M. Mäkyänen and M. Hallikainen, "Investigation of C- and X-band backscattering signatures of the Baltic Sea ice," *Int. J. Remote Sens.*, vol. 25, no. 11, pp. 2061–2086, 2004.
- [24] M. Mäkyänen, T. Manninen, M. Similä, J. Karvonen, and M. Hallikainen, "Incidence angle dependence of the statistical properties of the C-band HH-polarization backscattering signatures of the Baltic Sea ice," *IEEE Trans. Geosci. Remote Sens.*, vol. 40, no. 12, pp. 2593–2605, Dec. 2002.



Marko P. Mäkyänen (S'98–M'01) received the M.Sc. (Tech.) and Lic.Sci. (Technology) degrees in electrical engineering from the Helsinki University of Technology, Espoo, Finland, in 1994 and 1999, respectively. He is currently working toward the Doctor of Science degree in technology at the Helsinki University of Technology.

He is currently a Senior Teaching Assistant with the Laboratory of Space Technology, Helsinki University of Technology. His main research interest is the remote sensing of the Baltic Sea ice.

Markku H. Similä received the M.Sc. degree in mathematics from the University of Helsinki, Helsinki, Finland, in 1982.

Since 1990, he has been a Research Scientist with the Finnish Institute of Marine Research, Helsinki. His research area is SAR-based ocean remote sensing, especially sea ice mapping. His research interests are in statistical interpretation models for remote sensing radar data and analysis of images through different mathematical representations.



A. Terhikki Manninen received the M.Sc. (Tech.) degree (with distinction) in low-temperature physics, the Lic.Sci.Tech. degree in semiconductor physics, and the Dr.Phys. degree in remote sensing from the Helsinki University of Technology, Espoo, Finland, in 1981, 1986, and 1996, respectively.

From 1986 to 1994, she was a Research Scientist with the Finnish Institute of Marine Research, where her research centered around the active microwave remote sensing of Baltic Sea ice, especially the modeling of the surface description relevant for backscattering. From 1995 to 2002, she was a Senior Research Scientist with VTT Automation and VTT Information Technology, Remote Sensing, where her main interest was in surface roughness and forest microwave backscattering modeling. Since 2003, she has been a Senior Research Scientist with the Finnish Meteorological Institute, Helsinki. Her current research interests are related to the surface description of the Earth, such as broadband surface albedo and leaf area index.



Martti T. Hallikainen (M'83–SM'85–F'93) received the Engineering Diploma (M.Sc.) and the Dr.Sci.Tech. degree from the Helsinki University of Technology (TKK), Espoo, Finland, in 1971 and 1980, respectively.

Since 1987, he has been a Professor of space technology with the Helsinki University of Technology. In 1988, he established the TKK Laboratory of Space Technology, and currently serves as its Director. In 1993–1994, he was a Visiting Scientist with the Institute for Remote Sensing Applications, European Union's Joint Research Centre, Ispra, Italy. From 1981 to 1983, he was a Post-doctoral Fellow with the Remote Sensing Laboratory, University of Kansas. He was awarded with an Asla-Fulbright scholarship for graduate studies at the University of Texas at Austin in 1974–1975. His research interests include the development of microwave sensors for airborne and spaceborne remote sensing, development of methods to retrieve the characteristics of geophysical targets from satellite and airborne measurements, and cryospheric applications of remote sensing. His team is currently involved in the development of the L-band synthetic aperture radiometer MIRAS for the ESA SMOS satellite and a similar airborne instrument (HUT-2D) for the Laboratory's research aircraft.

Dr. Hallikainen has been a member of the IEEE Geoscience and Remote Sensing (GRSS) Administrative Committee since 1988 and served as President of IEEE GRSS in 1996–1997. He was the General Chair of the IGARSS'91 Symposium and the Guest Editor of the Special IGARSS'91 Issue of the IEEE TRANSACTIONS ON GEOSCIENCE AND REMOTE SENSING (TGARS). He was an Associate Editor of TGARS in 1992–2002. He has been the Vice President of the International Union of Radio Science (URSI) since 2005 and served as the Chair of URSI Commission F in 2002–2005. He has been a National Official Member of URSI Commission F since 1988 and was the Chair of URSI Finnish National Committee in 1997–2005. He has been the Vice Chair of the Finnish National Committee of COSPAR since 2000. He was a member of the European Space Agency's (ESA) Earth Science Advisory Committee in 1998–2001. He is a national delegate to the ESA Earth Observation Data Operations Scientific and Technical Advisory Group (DOSTAG) since 1995. He has been a member of the European Association of Remote Sensing Laboratories (EARSel) Council since 1985. He was the Secretary General of EARSel in 1989–1993 and the Chairman of the Organizing Committee for the EARSel 1989 General Assembly and Symposium. He has been a member of the Advisory Committee for the European Microwave Signature Laboratory of the European Union's Joint Research Centre since 1992. He was the recipient of three IEEE GRSS awards: 1994 Outstanding Service Award, IGARSS'96 Interactive Paper Award, and 1999 Distinguished Achievement Award. He was awarded the Microwave Prize for the best paper in the 1992 European Microwave Conference and the IEEE Third Millennium Medal in 2000.



Juha A. Karvonen received the M.Sc. degree in engineering and the Lic.Sci.Tech. degree from the Helsinki University of Technology (TKK), Espoo, Finland, in 1991 and 1996, respectively. He is currently working toward the Ph.D. degree in computer and information science at TKK.

He is currently a Research Scientist with the Finnish Institute of Marine Research, Helsinki. His research interests are signal and image processing, pattern recognition, intelligent systems, and automated interpretation of sensor, especially SAR, data.